

This is the accepted manuscript made available via CHORUS. The article has been published as:

Quantum-fluctuation-stabilized orthorhombic ferroelectric ground state in lead-free piezoelectric $(\text{Ba,Ca})(\text{Zr,Ti})\text{O}_3$

Alireza Akbarzadeh, Kumar Brajesh, Yousra Nahas, Naveen Kumar, Sergei Prokhorenko, Diptikanta Swain, Sergey Prosandeev, Raymond Walter, Igor Kornev, Jorge Íñiguez, Brahim Dkhil, Rajeev Ranjan, and L. Bellaiche

Phys. Rev. B **98**, 104101 — Published 4 September 2018

DOI: [10.1103/PhysRevB.98.104101](https://doi.org/10.1103/PhysRevB.98.104101)

Quantum-fluctuation-stabilized orthorhombic ferroelectric ground state in lead-free piezoelectric (Ba,Ca)(Zr,Ti)O₃

Alireza Akbarzadeh¹, Kumar Brajesh², Yousra Nahas¹, Naveen Kumar², Sergei Prokhorenko¹, Diptikanta Swain³, Sergey Prosandeev^{1,4}, Raymond Walter¹, Igor Kornev⁵, Jorge Íñiguez⁶, Brahim Dkhil⁵, Rajeev Ranjan² and L. Bellaiche¹

¹*Physics Department and Institute for Nanoscience and Engineering,*

University of Arkansas, Fayetteville,

Arkansas 72701, USA

²*Department of Materials Engineering,*

Indian Institute of Science,

Bangalore-560012, India

³*Solid State Structural Chemistry Unit,*

Indian Institute of Science,

Bangalore-560012, India

⁴*Institute of Physics and Physics Department of Southern,*

Federal University, Rostov-na-Donu 344090, Russia,

⁵*Laboratoire Structures,*

Propriétés et Modélisation des Solides,

CentraleSupélec, CNRS-UMR8580,

Université Paris-Saclay,

91190 Gif-sur-Yvette, France

⁶*Materials Research and Technology Department,*

Luxembourg Institute of Science and Technology,

(LIST), 5 avenue des Hauts-Fourneaux,

L-4362 Esch/Alzette, Luxembourg

Abstract

We numerically investigate the phase diagram of the giant-piezoelectric $(1 - x)\text{Ba}(\text{Zr}_{0.2}\text{Ti}_{0.8})\text{O}_3 - x(\text{Ba}_{0.7}\text{Ca}_{0.3})\text{TiO}_3$ system, treating the ions either as classical objects (via classical Monte-Carlo or CMC simulations) or quantum mechanically (via Path-integral Quantum Monte-Carlo or PI-QMC simulations). It is found that PI-QMC not only provides a better agreement with available experimental data for the temperature-composition phase diagram but also leads to the existence of an orthorhombic ground state in a narrow range of composition, unlike CMC that “only” yields ground states of rhombohedral or tetragonal symmetry. X-ray powder diffraction experiments are further conducted at 20 K. They confirm the occurrence of a quantum-fluctuation-induced orthorhombic state for some compositions and therefore validate the PI-QMC prediction. The role of quantum effects on the local structure, such as the annihilation of a homogeneous rhombohedral system in favor of an inhomogeneous mixing of orthorhombic and rhombohedral clusters, is also documented and discussed.

PACS numbers: 02.70.Ss, 77.80.bg, 61.05.C-, 81.30.Bx, 77.84.Lf

I. INTRODUCTION

Ever since its discovery in 2009, the extraordinary piezoelectric response ($d_{33} \simeq 600$ pC/N) of $(1 - x)\text{Ba}(\text{Zr}_{0.2}\text{Ti}_{0.8})\text{O}_3 - x(\text{Ba}_{0.7}\text{Ca}_{0.3})\text{TiO}_3$ solid solutions (to be denoted as BCTZ- x in the following) has attracted a lot of attention among the few lead-free alternatives (see, e.g., Refs. [1–7] and therein). While its non-toxicity offers promise for the design of eco-friendly piezoelectric-based devices, which is in line with various international incentives^{8,9}, the explanation of its remarkable piezoelectric response at room temperature has remained a challenge. An important aspect of BCTZ- x is its temperature-*versus*-composition phase diagram since it can exhibit three different ferroelectric phases (namely, tetragonal $P4mm$, orthorhombic $Amm2$ and rhombohedral $R3m$) in addition to a paraelectric cubic state. This imparts certain characteristics to the system such as phase convergence region, where different ferroelectric phases meet with the paraelectric cubic state¹ or even coexist inside the sample^{5,6}. The large piezoelectric response at room temperature is often associated with the proximity of a $P4mm - Amm2$ phase boundary to this convergence region, resulting in reduced anisotropy energy, large polarization and enhanced elastic softening⁴. A recent study also shows that the unique role of Ca in these systems lies in significantly reducing the spontaneous lattice strain without compromising the spontaneous polarization¹⁰.

While the existence of the $Amm2$ phase in a narrow temperature window around 300 K has been recognized as an important factor in imparting large piezoelectric response for some compositions (such as $x=0.50$) in this system⁷, there are still some questions surrounding this orthorhombic $Amm2$ state. For example, if one extrapolates the experimental phase diagram of BCTZ- x measured in Ref. [2] to low temperatures, the ever increasing (with composition) width of the $Amm2$ phase region suggests this phase to be the ground state (i.e., the phase of lower energy at zero Kelvin) in a very wide concentration, namely $0.65 < x < 0.95$. However, such latter ground-state symmetry for such large compositional window is rather surprising, when recalling that $Amm2$ has been invoked to be the ground state of some ferroelectric systems (e.g., for some hydrostatic pressure in BaTiO_3 ^{11,12} and for some compositions in the Zr-lacking $(\text{Ba,Ca})\text{TiO}_3$ system where Fu et al.¹³ discovered the anomalous phase transition thanks to effects of quantum fluctuations).

As a matter of fact, such fluctuations can, e.g., annihilate one polarization's component of the

rhombohedral $R3m$ ($|P_x| = |P_y| = |P_z|$) state in favor of $Am\bar{m}2$ ($|P_x| = |P_y| \neq 0, |P_z| = 0$). Interestingly, we are not aware that quantum effects have ever been predicted or measured to be of relevance in $\text{BCTZ}-x$. Moreover, if they do play a role in the stabilization of $Am\bar{m}2$ as ground state in these solid solutions, one may also wonder if they have any effect on the local (rather than macroscopic) structure of $(1-x)\text{Ba}(\text{Zr}_{0.2}\text{Ti}_{0.8})\text{O}_3-x(\text{Ba}_{0.7}\text{Ca}_{0.3})\text{TiO}_3$ too, especially in light of the fact that Ref. [7] numerically found a correspondence between local structure and enhancement of electromechanical properties.

The goal of this paper is to develop and use atomistic simulations, altogether with obtaining and analyzing X-ray diffraction patterns, to investigate roles of quantum fluctuations on macroscopic and microscopic properties of $\text{BCTZ}-x$. As we are going to see, these vibrations indeed result in the stabilization of an orthorhombic $Am\bar{m}2$ phase as the ground state of $(1-x)\text{Ba}(\text{Zr}_{0.2}\text{Ti}_{0.8})\text{O}_3-x(\text{Ba}_{0.7}\text{Ca}_{0.3})\text{TiO}_3$, but only for a narrow range of compositions – as consistent with their quantum nature (which plays a more important role only when the temperature is getting smaller). These quantum fluctuations are also found to dramatically affect the local structure in this narrow compositional window, via the suppression of certain types of clusters in favor of clusters of other symmetries.

This paper is organized as following: Section II provides details about the numerical and experimental methods used here. Sections III and IV reports and gives further insight into our results, respectively. Finally, a conclusion is given in Section V.

II. METHODOLOGY

A. Effective Hamiltonian

Regarding the numerical method we developed and used here, we first select two different x compositions, namely $x=0.50$ and 0.40 , for $\text{BCTZ}-x$ solid solutions. An effective Hamiltonian (H_{eff}) is built for both of these concentrations, adopting the virtual crystal approximation (VCA)^{14,15}. In other words, we mimic $\langle A \rangle \langle B \rangle \text{O}_3$ simple systems, for which the virtual $\langle A \rangle$ atom involves a compositional average of Ba and Ca potentials (with, e.g., a 85% and 15% contribution, respectively, for $\text{BCTZ}-0.5$) while the average $\langle B \rangle$ atom is built from a mixing of the Zr and Ti

potentials (with, e.g., a 10% and 90% contribution, respectively, for BCTZ–0.5)⁷.

As in Ref. [16], the degrees of freedom of this H_{eff} are the local soft mode \mathbf{u}_i of each 5-atom unit cell (which is proportional to the electric dipole moment of cell i), the homogeneous strain tensor, and inhomogeneous-strain-related dimensionless displacements, $\{\mathbf{v}_i\}$. Technically, the $\{\mathbf{u}_i\}$'s and $\{\mathbf{v}_i\}$'s are centered on the $\langle B \rangle$ and $\langle A \rangle$ sites, respectively. The analytical expression of the total internal energy of this effective Hamiltonian is the one provided in Ref. [16] for pure BaTiO₃, and therefore contains a local-mode self-energy, a long-range dipole-dipole interaction, a short-range interaction between soft modes, an elastic energy, and an interaction between the local modes and local strains. Note that we further extended the local-mode self energy given in Ref. [16] by including an isotropic sixth-order term (as we will see later this addition is essential to be able to reproduce the entire phase diagram of BCTZ– x , that is for x ranging between 0 and 1). Thereby, the new local-mode self-energy is given by:

$$E_{\text{self}} = \sum_i \{ \kappa_2 u_i^2 + \alpha u_i^4 + \gamma (u_{i,x}^2 u_{i,y}^2 + u_{i,y}^2 u_{i,z}^2 + u_{i,z}^2 u_{i,x}^2) + \delta u_i^6 \} \quad (1)$$

where the sum runs over all the $\langle B \rangle$ sites, and $u_{i,k}$, with $k = x, y, z$ are the Cartesian components of \mathbf{u}_i in the orthonormal basis formed by the [100], [010] and [001] pseudo-cubic directions. κ_2 , α and γ are parameters, that are in a first step determined, along with the other coefficients of the effective Hamiltonian, by performing density functional theory (DFT) calculations within the VCA approach¹⁵ on small $\langle A \rangle \langle B \rangle \text{O}_3$ cells (less than 20 atoms) to model BCTZ–0.5 and BCTZ–0.4 (choosing and keeping $\delta=0$ for these two systems).

This effective Hamiltonian^{7,14–17} is then employed in different kinds of Monte-Carlo (MC) simulations: classical MC (CMC) and path integral quantum MC (PI-QMC)^{18,19}. PI-QMC takes into account the quantum-mechanical fluctuations of the atoms and thus yields, unlike CMC simulations, realistic results when such fluctuations are dominant over thermal vibrations. To mimic quantum effects in PI-QMC, each five-atom cell interacts with its images at neighboring imaginary times through a spring-like potential while all the five-atom cells interact with each other at the same imaginary time through the internal potential given by the effective Hamiltonian. The product TP , where T is the simulated temperature and P is the number of imaginary time slices (also termed Trotter number), controls the accuracy of the PI-QMC calculation. In all our simulations, we use $TP \approx 1200$ to obtain sufficiently converged results. We start with $P=1$, i.e., CMC simulations and then successively increase the Trotter number. For example at $T=5\text{K}$, the trotter

number is increased as follows: $1 \rightarrow 3 \rightarrow 6 \rightarrow 12 \rightarrow 24 \rightarrow 48 \rightarrow 96 \rightarrow 192$.

Both CMC and PI-QMC simulations using the total energy of the effective Hamiltonian are conducted on large supercells (of $12 \times 12 \times 12$ dimensions) to mimic BCTZ–0.5 and BCTZ–0.4, assuming that the δ parameter of Eq. (1) vanishes in these systems – as consistent with first-principle calculations we performed. During the PI-QMC simulations, κ_2 is adjusted in order to fit the experimental value of the Curie temperature^{1,2,4} (since H_{eff} techniques can underestimate the paraelectric-to-ferroelectric transition temperature^{16,17}) and γ is slightly varied to reproduce the measured *lowest* transition temperature observed in Refs. 2 and 4 for BCTZ– x with $x=0.5$ and 0.4 .

Having determined all the H_{eff} parameters for these two latter compositions, we then extract those for any composition ranging between 0 and 1 by simply linearly interpolating or extrapolating the coefficients of the two compositions of 0.40 and 0.50. However, we also numerically realized that one needs to further introduce finite values of the δ parameter of Eq. (1) in order to be able to accurately describe the phase diagram for small or large compositions, likely because these compositions are the ones that are further away from our initial choices of $x = 0.5$ and 0.4 and/or because such limiting compositions seem to exhibit a strong first-order transition between paraelectric and ferroelectric phases. Practically, we varied and calibrated the parameter δ entering such isotropic sixth-order term for four compositions, that are $x = 0, 0.2, 0.8$, and 1 , so that the Path-Integral quantum Monte-Carlo (PI-QMC) predictions are close to the available experimental values of the Curie transition temperature for all these compositions^{1,2}. For instance, using a value of $\delta = 0.2$ for the composition of $x = 1$ leads to PI-QMC predicting a tetragonal-to-cubic paraelectric transition temperature of 380 ± 5 K when heating the system *versus* 460 ± 5 K for $\delta = 0$, while the corresponding measured data is ≈ 391 K¹. We then used a linear extrapolation or interpolation to determine non-zero and positive values of δ for compositions $x \leq 0.33$ and $x > 0.6$ (while δ is chosen to be zero for compositions in-between).

The resulting set of all compositionally-dependent H_{eff} parameters is then used in both the CMC and PI-QMC simulations for BCTZ– x with x varying between 0 and 1 ((note that the present κ_2 parameters are about $\approx 4\%$ lower than those used in Ref. [7], because we presently fit our PI-QMC results to the measured Curie temperatures for $x = 0.5$ and 0.4 while Ref. [7] fitted the CMC numerical data to these experimental Curie temperatures).

B. XRD measurements

We also decided to perform structural analysis to check the validity of our predictions. We synthesized ceramic specimens of $(1 - x)\text{Ba}(\text{Zr}_{0.2}\text{Ti}_{0.8})\text{O}_3 - x(\text{Ba}_{0.7}\text{Ca}_{0.3})\text{TiO}_3$ with $x = 0.70, 0.80, 0.82, 0.835, 0.845, 0.87$ and 0.89 using the synthesis process reported before in Ref. [5]. To determine the ground state structure of these compositions, we collected x-ray powder diffraction data at 20 K using laboratory x-ray powder diffractometer (Cu-K α 1 radiation), and conducted a Rietveld analysis using the Fullprof Software²⁰. The monochromatic (Cu-K α 1) x-ray beam in combination with the high resolution optics and rotating anode target ensured very high quality diffraction data. The good resolution in combination with the excellent peak to background ratio even at high angles enabled us to identify the characteristic peaks of the different phases (tetragonal, orthorhombic and rhombohedral) in an unambiguous manner. This aspect is very important to ensure, especially for identification of the orthorhombic and rhombohedral ferroelectric phases in BaTiO₃-based piezoelectrics as they exhibit almost similar pseudocubic lattice parameters^{6,21}. This makes the identification of the phases difficult, more so when they coexist.

III. RESULTS

A. Phase diagram: PIQMC vs. CMC

We employ such effective Hamiltonians to determine the phase stability as a function of temperature for the entire composition space, i.e, $0 \leq x \leq 1$, by analyzing the behavior of the Cartesian components of the spontaneous polarization *versus* temperature. The results of these analyses are shown in the phase diagram of Figure 1, both for the CMC and PI-QMC simulations. Note that a phase diagram of BCTZ- x was also reported in a recent study by Nahas et al.⁷, but only for compositions $0.25 \leq x \leq 0.65$ and for CMC simulations.

Four structural phases occur in this phase diagram for both CMC and PI-QMC simulations: one paraelectric cubic state of $Pm\bar{3}m$ symmetry at high temperature for any composition, and three ferroelectric phases, namely tetragonal $P4mm$, orthorhombic $Amm2$, and rhombohedral $R3m$. One can first see that the PI-QMC simulations provide lower transition temperatures than CMC calculations, which is a feature that has been previously found in other systems and which is also consistent with the fact that quantum effects tend to promote disorder and can even suppress

ferroelectric phases in some materials (such as SrTiO_3 or KTaO_3)^{18,19}. For instance, for the composition of $x = 0.5$, PI-QMC (CMC) simulations lead to the following transition temperatures: 370 K (380 K) for $Pm\bar{3}m$ -to- $P4mm$; 300 K (320 K) for $P4mm$ -to- $Amm2$; and 270 K (285 K) for $Amm2$ -to- $R3m$, respectively. The experimental data reported in Ref. [2] for these three observed transitions are approximately 366 K, 301 K, and 272 K, respectively, which are therefore all very close to the PI-QMC data, especially when realizing that the error bars on the calculated transition temperatures are $\pm 5\text{K}$.

Figure 1 also shows that, for compositions $0.0 \leq x \leq 0.33$, CMC and PI-QMC computations both predict a single paraelectric cubic-to-ferroelectric rhombohedral transition when heating $\text{BCTZ}-x$, which is in line with observations too^{2,4}— with, once again, the PI-QMC data agreeing quantitatively well with the measurements. Moreover, results from CMC and PI-QMC in Fig. 1 further indicate that a cubic paraelectric-to-tetragonal ferroelectric transition occurs for compositions $0.34 \leq x \leq 1$, from the lowest $355 \pm 5 \text{ K}$ (respectively, $370 \pm 5 \text{ K}$) at $x = 0.34$ to the highest $380 \pm 5 \text{ K}$ (respectively, $400 \pm 5 \text{ K}$) at $x = 1$, as predicted in PI-QMC (respectively, CMC) simulations and as consistent with experiments^{1,2,4}. Note that, in the region extending from $x=0.34$ to $\simeq 0.37$ and near temperatures of around 355 K and 370 K for the PI-QMC and CMC simulations, respectively, the $Pm\bar{3}m$, $P4mm$, $Amm2$ and $R3m$ phases are all close to each other. As shown by Fig. 1, the (composition, temperature) position of this specific area predicted by the PI-QMC method is therefore rather close to the one observed by Liu et al.¹ and that is centered around ($x \sim 0.32$, $T \sim 330 \text{ K}$), even if the existence of an orthorhombic phase was overlooked in Ref. [1] for larger compositions (such as $x = 0.4$) before being observed by Keeble *et al.*².

In addition and at low temperatures, CMC predicts the existence of rhombohedral and orthorhombic phases for compositions $0.37 \leq x \leq 0.917$ with a rhombohedral ground state. In contrast, PI-QMC simulations show that, at low temperatures, the ground state will become orthorhombic for compositions $0.83 < x < 0.86$, and tetragonal for $x \geq 0.86$. Such numerical findings reveal that quantum fluctuations suppress the ferroelectric rhombohedral ground state in favor of an orthorhombic one for x ranging between 0.83 and 0.86, and even suppress both orthorhombic and rhombohedral states in favor of a tetragonal phase for concentration varying between 0.86 and 0.917! As a result, the CMC simulations predict that a single paraelectric cubic-to-ferroelectric tetragonal-transition exists when decreasing the temperature in $\text{BCTZ}-x$

with x being larger than 0.917, while such single transition occurs for any x higher than 0.86 when quantum effects are accounted for.

The importance of quantum effects in BCTZ- x at low temperature can be further asserted from the fact depicted in Fig. 1 that the transition temperatures lower than, e.g., 160 K can be very well fitted by the theoretical expression $T_c \propto (x_c - x)^{1/\beta}$, where T_c is the Curie transition temperature, x is the concentration, x_c is the critical concentration, and the critical exponent β is precisely 2 in the quantum limit²². Note that fitting by this formula also provides $x_c = 0.830$ and 0.858 for the $R3m$ -to- $Amm2$ and the $Amm2$ -to- $P4mm$ transitions, respectively, which are very close to our aforementioned numerically determined two compositional values of $\simeq 0.83$ and 0.86 delimiting the orthorhombic ground state. Note also that Ref. [2] correctly guessed that the orthorhombic $Amm2$ state can be the ground state of BCTZ- x but its assumed compositional range of stability (that is between $0.65 \leq x \leq 0.95$) is much larger than what we numerically find here.

Such discrepancy relies on the fact that, unlike Ref. [13] in Zr-lacking (Ba,Ca)TiO₃ system, the authors of Ref. [2] probably did not realize that, most likely, an orthorhombic $Amm2$ phase can only be the ground state of ferroelectric systems because of subtle quantum effects, which suggests that its range of stability will be a narrow one. In fact, we are not aware that such quantum effects, in general, and the existence of an orthorhombic ground state, in particular, have ever been mentioned and measured in BCTZ- x .

B. Phase diagram: XRD measurements

In conformity with the phase diagram of Fig. 1, the XRD patterns for all the compositions show tetragonal structure at room temperature. As mentioned earlier, to determine the ground state we collected XRD data at 20 K. The best way to identify the rhombohedral and orthorhombic distortions is by scrutinizing (visually!) the splitting of characteristic pseudocubic Bragg profiles $\{h00\}_{pc}$, $\{hh0\}_{pc}$ and $\{hhh\}_{pc}$. For example, for a tetragonal distortion the $\{h00\}_{pc}$ is split into two with certain characteristic intensity ratio, while the $\{hhh\}_{pc}$ is a singlet. The reverse is the case for a rhombohedral distortion. Similarly, the orthorhombic distortion gives certain characteristic

features in the diffraction pattern. Because of the weak distortion, the splitting of the $\{111\}_{pc}$ and $\{200\}_{pc}$ profiles is not very clear. We therefore focused our attention on the higher order profiles $\{222\}_{pc}$ and $\{400\}_{pc}$. Although the intensity of these Bragg profiles are considerably weaker than their corresponding lower order counterparts, still the peak to background ratio of the data is sufficiently good. For example, the peak count of the $\{222\}_{pc}$ is 1300 and the background is 50. For $x = 0.89$, the singlet nature of $\{222\}_{pc}$ and the doublet in the $\{400\}_{pc}$ confirm the $P4mm$ structure. As x decreases to 0.87, a weak shoulder appears on the left of the tetragonal (400) peak, as seen in Fig. 2(e). This is a signature of the orthorhombic (O) phase. The same feature can be seen for x down to 0.825 with slightly enhanced intensity of the O peak marked in Fig. 2(d). Rietveld analysis, carried out for the entire diffraction pattern (20 - 120) confirmed the $P4mm + Amm2$ phase coexistence of $x = 0.87$ and 0.825 (see Fig. 3(d)). As x decreases to $x = 0.82$, not only the intensity of the O-peak (and also on the left of the O-peak) is further enhanced, but also a weak hump appears (marked by R in Fig. 2(c)) in the $\{222\}_{pc}$ profile. The intensity of the R peak increases considerably for $x = 0.80$. Concomitantly, the shape of $\{400\}_{pc}$ is significantly altered due to appearance of a new peak (also marked by R) in between and almost equidistant from the two tetragonal (004) and (400) peaks. We confirmed by Rietveld analysis that the additional R peaks in $x = 0.82$ and 0.80 arise due to the rhombohedral $R3m$ phase, see Fig. 3(c). The XRD patterns of $x = 0.82$ and 0.80 could be fitted satisfactorily with $P4mm + Amm2 + R3m$ phase (note that the refined structural parameters of the three phases are given in Table I for BCTZ-0.82). In contrast to $x = 0.80$, the $\{400\}_{pc}$ profile of $x = 0.70$ is a singlet, suggesting the absence of the $Amm2$ and $P4mm$ phases (see Fig. 2(a)). This is confirmed by Rietveld analysis of this pattern by the single $R3m$ phase, as shown in Fig. 3(a). Table II reports resulting phase fraction of the different compositions at 20 K. Note that the tetragonal ($P4mm$) fraction does not exist for $x = 0.70$ (the only phase is $R3m$ for that composition), and then increases with increasing x from 0.80 to 0.87, until it becomes the only phase for compositions above 0.89, which is in line with the PI-QMC phase diagram of Fig. 1. The coexistence of the high temperature $P4mm$ and $Amm2$ phases at 20 K for $x = 0.80$ is likely due to kinetic factors which makes the $P4mm \rightarrow Amm2 \rightarrow R3m$ transitions very sluggish at low temperatures⁵. Ignoring the coexisting metastable high-temperature ferroelectric phase(s), our experiments confirm that $Amm2$ is the equilibrium state of BCTZ- x at 20 K in the composition interval $0.825 < x < 0.87$ (in other words, one can decide that $Amm2$ should be the real ground state of BCTZ- x for compositions at which it coexists only with the $P4mm$ state because of the sluggish nature of the $P4mm - Amm2$

transition, that is, without such sluggish character, $P4mm$ would have completely transformed into $Amm2$ when cooling down the samples). This is in remarkable agreement with our PI-QMC prediction of the $Amm2$ ground state for the narrow composition range $0.83 < x < 0.86$. Our experimental analysis therefore supports our exciting discovery of quantum-fluctuation-stabilized $Amm2$ ground state in this system.

IV. DISCUSSIONS AND FURTHER INSIGHTS

A. Fluctuation Analysis: Quantum vs. Thermal

Let us now concentrate on the composition of $x = 0.845$, for which the associated δ is 0.1225. Figures 4 (a) and (b) report the averaged Cartesian components of the polarization, $\langle P_k \rangle$ (with $k = x, y, z$ being along the pseudo-cubic $\langle 001 \rangle$ axes), *versus* temperature, when heating the system for that composition during the CMC and PI-QMC simulations, respectively. Note that we typically run 200,000 Monte-Carlo (MC) sweeps, in order to accurately obtain transition temperatures.

The CMC simulations predict three transitions (for which critical temperatures are calculated within ± 5 K variations) when heating the system from low to high temperatures, that are (1) ferroelectric rhombohedral $R3m$, for which all components are finite and equal to each other, to the ferroelectric orthorhombic $Amm2$, with $\langle \mathbf{P}_z \rangle = 0$ while $\langle \mathbf{P}_x \rangle = \langle \mathbf{P}_y \rangle$ remain non-zero, at $\simeq 75$ K; (2) $Amm2$ -to-ferroelectric tetragonal $P4mm$ at $\simeq 115$ K with $\langle \mathbf{P}_x \rangle$ being the only finite Cartesian component of the polarization; and (3) tetragonal $P4mm$ -to- $Pm\bar{3}m$ paraelectric cubic, with $\langle \mathbf{P}_x \rangle = \langle \mathbf{P}_y \rangle = \langle \mathbf{P}_z \rangle = 0$ at $\simeq 385$ K. On the other hand, PI-QMC simulations result in only two phase transitions, that are $Amm2$ -to- $P4mm$ around $\simeq 65$ K, and $P4mm$ -to- $Pm\bar{3}m$ around 370 K. In other words, quantum effects not only push down the $P4mm$ -to- $Pm\bar{3}m$ transition temperature by around ≈ 15 K but also completely suppress the rhombohedral phase.

Let us further investigate the roles of quantum mechanical fluctuations of the atoms for that composition of $x = 0.845$, by calculating the contribution of thermal *versus* quantum fluctuations for the polarization, as similar to what was done in Ref. [18]. Specifically, letting $p_k(i, s, t)$, with $k = x, y, z$, representing the Cartesian component of the local dipole on lattice site i , imaginary times (Trotter slices) s and Monte Carlo sweep t during the PI-QMC simulations, then thermal

fluctuations can be obtained using:

$$(\Delta p_k^{thermal})^2 = \langle \langle p_k^2 \rangle_s \rangle_{i,t} \quad (2)$$

while the total fluctuation is given by:

$$(\Delta p_k^{total})^2 = \langle p_k^2 \rangle_{i,s,t} \quad (3)$$

where bracket $\langle \dots \rangle$ indicates the averages over Trotter number s , lattice sites i , and/or Monte Carlo sweeps t . Note that we used here the last configuration of the Monte Carlo sweeps to compute these fluctuations. Quantum fluctuations can then be obtained via the difference between total and thermal fluctuations, that is:

$$(\Delta p_k^{Quantum})^2 = (\Delta p_k^{total})^2 - (\Delta p_k^{thermal})^2 \quad (4)$$

Panels (a), (b), (c) of Figs. 5 show the square root of all these fluctuations (i.e., total, thermal and quantum) for the x , y and z components of the local dipoles, respectively, after conversion to have them in C/m^2 units – that is, to render them in units of polarization rather than units of electric dipoles. For any of such Cartesian components, the thermal and total fluctuations are almost equal to each other above 370 K, that is in the cubic paraelectric state, implying that quantum fluctuations are very small for these high temperatures. Moreover, when $65 \leq T < 370$ K, that is when a tetragonal phase $P4mm$ occurs with a polarization developing along the x -axis (See Fig. 4(b)), $\Delta p_x^{thermal}$ and Δp_x^{total} (i.e., the thermal and total fluctuations of the local electric dipoles along the polarization axis) are still close to each other, and both increase when the temperature decreases. On the other hand, $\Delta p_y^{thermal}$ and $\Delta p_z^{thermal}$ not only decrease meanwhile but also begin to differ more and more from their corresponding total fluctuations. As a result, quantum fluctuations of the electric dipoles along the two Cartesian axes being orthogonal to the polarization direction become more significant as the temperature is reduced in the $P4mm$ state. At about 65 K, the x and y -components of the thermal fluctuations suddenly decrease and increase when decreasing the temperature, respectively, in order to become equal to each other for temperatures below 65 K – which is the region for which the ground state is orthorhombic $Amm2$ and has a polarization lying along the pseudo-cubic $[110]$ direction, as shown in Fig. 4(b). Note that $\Delta p_x^{thermal}$ and $\Delta p_y^{thermal}$ are much larger than $\Delta p_x^{Quantum}$ and $\Delta p_y^{Quantum}$, respectively, in that $Amm2$ state, therefore indicating that quantum vibrations have relatively small effects on local electric dipoles along the x and y -axes there. On the other hand, $\Delta p_z^{Quantum}$ overcomes

the thermal fluctuations along the (non-polar) z axis below 65K, with $\Delta P_z^{thermal}$ even becoming negligible as the system is further cooled down. In other words, quantum fluctuations are now the dominant effect for the fluctuations of the z -component of the electric dipoles at low temperatures – therefore explaining why the rhombohedral $R3m$ phase is killed, in favor of the orthorhombic $Am\bar{m}2$ phase, by quantum effects in BCTZ-0.845. Note that, similarly, in incipient ferroelectrics SrTiO_3 and KTaO_3 , such overcome of quantum to thermal fluctuations have been shown to suppress the paraelectric-to-ferroelectric transition^{18,23}, and that quantum fluctuations are dominant there for temperatures lower than 100 K^{18,23,24}.

Let us now focus on such fluctuations, but for different compositions at a fixed temperature of 5K, as shown in Figs 6(a)-(c) for concentrations $0.80 < x < 0.87$. One can see in that, for $0.80 \leq x \leq 0.83$, the *thermal* fluctuations along x, y, z -axes are all equal to each other and $\approx 0.25 \text{ C/m}^2$, while the quantum fluctuations are much smaller and about 0.1 C/m^2 . Such features are consistent with the fact that the quantum vibrations are not strong enough to “kill” the rhombohedral ground state for these compositions (see Figure 1). On the other hand, the thermal fluctuations of the z -component of the electric dipoles suddenly decrease when the composition passes through 0.83 and become rather negligible for $0.83 < x < 0.86$, while its quantum fluctuations slightly increase to become nearly identical to the total fluctuations meanwhile (note also that the thermal fluctuations of the x - and y -components of the electric dipoles are still equal to each other and larger not only than their corresponding values for $0.8 \leq x \leq 0.83$ but also than their quantum fluctuations when $0.83 < x < 0.86$). Such striking behaviors are at the heart of the quantum-induced suppression of the $R3m$ state in favor of the $Am\bar{m}2$ orthorhombic phase as the ground state for these compositions $0.83 < x < 0.86$. Similarly, for concentrations above 0.86, the y -component of the electric dipoles, in addition to the z -component, also now wants to have vanishing thermal fluctuations, that is to have its quantum fluctuations taking over for the total fluctuations (while the thermal fluctuations of the x -component of the electric dipoles are enlarged with respect to smaller compositions while continuing to be close to their total fluctuations). As a result, quantum effects suppress both the orthorhombic and rhombohedral phases to make $P4mm$ the ground state for $0.86 < x < 0.917$ (as consistent with Fig. 1).

B. Cluster Analysis

Let us now further take advantage of our simulations in order to gain additional insights into BCTZ- x , in general, and the consequence of quantum effects on properties of such system, in particular. More precisely, we are interested to reveal how quantum vibrations can affect the local structure of this compound, especially because specific features of local structure (namely, a fragmented type of local structure and small strength of percolating clusters) have been previously linked with the occurrence of large piezoelectricity in this compound⁷. For that, we determined the percentage of dipoles belonging to clusters of tetragonal (T), Orthorhombic (O) and Rhombohedral (R) symmetry, within which dipoles nearly all lie along $\langle 001 \rangle$, $\langle 110 \rangle$ and $\langle 111 \rangle$ pseudo-cubic directions, respectively.

Such cluster analysis is technically done using the Hoshen-Kopelman algorithm²⁵ for the sole composition $x = 0.845$ (which falls in the middle of the stability range of the orthorhombic ground state according to our PI-QMC simulations). Such analysis is reported in Figs. 7a and 7b as a function of temperature below 80 K for CMC and PI-QMC computations, respectively. The CMC simulations predict that (i) a percolating O cluster exists at 80 K inside which dipoles lie along the polarization direction, and that constitutes $\sim 84\%$ of the supercell; and (ii) for any temperature smaller than 75 K, all dipoles belong to a single R cluster with phase fraction larger than $\sim 94\%$, therefore making the system quite homogeneous and adopting a rhombohedral $R3m$ polar state – as evidenced in the inset of Fig. 7(a) for the temperature of 60 K. On the other hand, the analysis from PI-QMC simulations shows that: (1) for temperatures ranging between 70 and 80 K, the tetragonal $P4mm$ state exhibits almost 80% of its dipoles lying along the polarization direction and therefore belonging to a T cluster, but also possesses a non-negligible number (namely, around 7%) of dipoles belonging to different types of O clusters (that is, O clusters for which the dipoles are parallel to different $\langle 110 \rangle$ directions); (2) for temperatures ranging between 35 K and 65 K, a mixture of a single type of O cluster (inside which dipoles are along a unique $\langle 110 \rangle$ direction) and of two types of R clusters (having two different $\langle 111 \rangle$ directions, whose average is precisely the polar axis of the single O cluster) also occurs, as shown in the inset of Fig. 7(b) for the temperature of 60 K. However, the O cluster is now majoritary, i.e., it occupies at least 86%, therefore resulting in a macroscopic orthorhombic $Amm2$ state rather than $R3m$; and (3) for temperatures smaller than 30 K, a single O cluster exists and fills up nearly all the supercell. Comparing Figs. 7a and 7b, and their insets, therefore reveals that quantum effects have large

implication on the local structure by, e.g., making the unique R cluster of the CMC simulations transforming into a mixture of T and O clusters for temperatures between 70 and 75 K and to a mixture of O and R clusters for temperatures between 35 K and 65 K within PIQMC simulations, in particular, and rendering such local structure more inhomogeneous, in general.

Note that we also applied electric fields of different magnitude along a $\langle 111 \rangle$ pseudo-cubic direction and computed, at 60K and for composition of 0.845, the resulting change of strain along that direction in both the CMC (homogeneous rhombohedral state) and PIQMC (inhomogeneous orthorhombic state) cases as shown in Figure 8. Piezoelectricity is then deduced from the slope of the strain-*versus*-electric field curve, and is found to be much higher in the PIQMC situation than in the CMC case (namely of the order of 81 pC/N in the former versus 6 pC/N in the latter). As *O* phase is intermediate between the *T* and *R* phases, such fact is in line with the polarization rotation mechanism, which is inherent to morphotropic boundaries of piezoelectric compositional oxides²⁶, in which piezoelectric properties are enhanced owing to a small energy difference between the local dipole positions along [001] and [111] directions. What we found here and what is extremely important for the effect observed, piezoelectric properties of oxides can be further drastically enhanced by melting large percolation domains to inhomogeneous local structures (which rotate polarization in small polar clusters much easier than in large polar clusters²⁷), as consistent with recent work of Refs. [28 and 29].

V. CONCLUSION

In summary, two types of atomistic effective Hamiltonian simulations (namely, classical vs. quantum-mechanical) are used to reveal that the quantum fluctuations of the atoms quantitatively, and also qualitatively, affect the phase diagram of BCTZ-*x*. These quantitative effects are changes in the value of the transition temperatures. Then, examples of qualitative effects are (1) the stabilization, via quantum fluctuations, of the *Amm2* orthorhombic phase as the ground state for a narrow compositional region; and (2) the modification of the local structure via the full suppression of clusters of some symmetry in favor of clusters of other symmetries. Our simulations results also emphasize on the importance of inhomogeneous local structures for enhancing piezoelectricity thanks to quantum fluctuations. The existence of a low-temperature *Amm2* state for some compositions is experimentally confirmed thanks to the analysis of X-ray patterns we

additionally conduct here. We thus hope that the present article offers a deeper knowledge of lead-free giant-response piezoelectric materials as well as the role of quantum lattice-dynamical effects at macroscopic and microscopic scales.

VI. ACKNOWLEDGMENTS

A.A, Sergei P., Sergey P. and L.B. thank the DARPA grant HR0011-15-2-0038 (MATRIX program). Sergey P. also appreciates support from RMES 3.1649.2017/4.6 and RFBR 18-52-00029 Bel.a. Y. N. acknowledges the ARO grant W911NF-16-1-0227. R.W. thanks the National Science Foundation Graduate Research Fellowship Program under Grant No. DGE-0957325 and the University of Arkansas Graduate School Distinguished Doctoral Fellowship. R. R acknowledges the support from the Science and Engineering Research Board (SERB) of the Department of Science and Technology, Govt. of India (Grant No. EMR/2016/001457). K. B gratefully acknowledges the award of National Post Doctoral Fellowship by Science and Engineering Research Board. We also acknowledge the FNR Luxembourg Grants FNR/P12/4853155/Kreisel (J.I.) and INTER/MOBILITY/15/9890527 GREENOX (L.B. and J.I.) and 16/1159210 MULTICALOR (B.D.). The authors thank Charles Paillard for useful discussions and the use of a software to compute tensors in different bases.

References

-
- ¹ W. Liu and Z. Ren, Phys. Rev. Lett. **103**, 257602 (2009).
 - ² D.S. Keeble, F. Benabdallah, P.A. Thomas, M. Maglione, and J. Kreisel, Appl. Phys. Lett. **102**, 092903 (2013).
 - ³ G. Tutuncu, Li Binzhi, K. Bowman, and J. L. Jones, *J. Appl. Phys.* **115**, 144104 (2014)
 - ⁴ M. Acosta, N. Khakpash, T. So,eya, N. Novak, W. Jo, H. Nagata, G.A. Rossetti Jr., J. Rödel Phys. Rev. B **91**, 104108 (2015).
 - ⁵ K. Brajesh, M. Abebe and R. Ranjan, Phys. Rev. B **94**, 104108 (2016).
 - ⁶ K. Brajesh, K. Tanwar, M. Abebe and R. Ranjan, Phys. Rev. B **92**, 224112 (2015).

- ⁷ Y. Nahas, A.R. Akbarzadeh, S. Prokhorenko, S. Prosandeev, R. Water, I. Kornev, J. Íñiguez, and L. Bellaiche, *Nature Communications* **8**, 15944 (2017).
- ⁸ European Commission, Directive 2002/95/EC of the European Parliament and of the Council of 27 January 2003 on the restriction of the use of certain hazardous substances in electrical and electronic equipment. *Off. J. Eur. Union L* **37**, 19 (2003).
- ⁹ European Commission, Directive 2011/65/EU of the European Parliament and of the Council of 8 June 2011 on the restriction of the use of certain hazardous substances in electrical and electronic equipment. *Off. J. Eur. Union L* **174**, 88 (2011).
- ¹⁰ M. Abebe, K. Brajesh, A. Mishra, A. Senyshyn and R. Ranjan *Phys. Rev. B* **96**, 014113 (2017).
- ¹¹ J. Íñiguez and D. Vanderbilt, *Phys. Rev. Lett.* **89** 115503 (2002).
- ¹² T. Ishidate, S. Abe, H. Takahashi, and N. Môri, *Phys. Rev. Lett.* **78** , 2397 (1997).
- ¹³ D. Fu, M. Itoh, S. Koshihara, T. Kosugi, and S. Tsuneyuki, *Phys. Rev. Lett.* **100**, 227601 (2008).
- ¹⁴ J.A. Van Vechten, *Phys. Rev. A* **182**, 891 (1969).
- ¹⁵ L. Bellaiche and D. Vanderbilt, *Phys. Rev. B* **61**, 7877 (2000).
- ¹⁶ W. Zhong, D. Vanderbilt, and K.M. Rabe, *Phys. Rev. Lett.* **73**, 1861 (1994); W. Zhong, D. Vanderbilt, and K.M. Rabe, *Phys. Rev. B* **52**, 6301 (1995).
- ¹⁷ L. Walizer, S. Lisenkov, and L. Bellaiche, *Phys. Rev. B* **73**, 144105 (2006).
- ¹⁸ W. Zhong and D. Vanderbilt, *Phys. Rev. B* **53**, 5047 (1996).
- ¹⁹ A.R. Akbarzadeh, L. Bellaiche, K. Leung, J. Íñiguez, and D. Vanderbilt, *Phys. Rev. B.* **70**, 054103 (2004).
- ²⁰ Rodrigues-J. Carvajal. FullPROF 2000 A Rietveld Refinement and Pattern Matching Analysis Program. France: Laboratories Leon Brillouin (CEA-CNRS).
- ²¹ A. Kalyani, H. Krishnan, A. Sen, A. Senyshyn, and R. Ranjan, *Phys. Rev. B* **91**, 024101 (2015).
- ²² U.T. Hochli and L.A. Boatner L. A., *Phys. Rev. B* **20**, 266, (1979).
- ²³ A.R. Akbarzadeh, *Simulating Quantum Effects in Ferroelectrics from First-Principles*, Doctoral Dissertation, University of Arkansas (2005).
- ²⁴ M. Vojta, *Rep. Prog. Phys.* **66**, 2069 (2003)
- ²⁵ J. Hoshen, R. Kopelman, *Phys. Rev. B* **14**, 3438 (1976).
- ²⁶ H. Fu, and R. Cohen, *Nature* **403**, 281 (2000).
- ²⁷ S. Prosandeev, B. Xu, and L. Bellaiche, *Phys. Rev. B* **98**, 024105 (2018)

- ²⁸ F. Li, D. Lin, Z. Chen, Z. Cheng, J. Wang, C.C. Li, Z. Xu, Q. Huang, X. Liao, L.-Q. Chen, T. R. ShROUT and S. Zhang, *Nature Materials* **17**, 349 (2018)
- ²⁹ B. Narayan, J. S. Malhotra, R. Pandey, K. Yaddanapudi, P. Nukala, B. Dkhil, A. Senyshyn, R. Ranjan, *Nature Materials* 17, 427 (2018).

Table's and Figures' Captions

FIG. 1. (color online): Temperature-versus-composition phase diagram of BCTZ- x , as predicted by PIQMC (filled circles) and CMC (open circles). The predicted transition temperatures are extracted (within a ± 5 K error bar) from the temperature evolution of polarization at fixed compositions. The solid blue lines show the fit of some critical transition temperatures (being below 160 K) into $T_C \propto (x_c - x)^{1/2}$, where x_c is a critical composition. The dashed and dotted lines are to guide the eye, and the box emphasizes the so-called phase convergence region (PCR). Note that experimental data of Refs. [1, 2, and 4] are also indicated in this phase diagram via the use of filled blue triangles, open red squares and filled pink triangles, respectively.

FIG. 2. (color online): X-ray (Cu-K α 1) powder diffraction profiles of pseudocubic $\{222\}_{pc}$ and $\{400\}_{pc}$ reflections of some BCTZ- x samples at 20 K. The R, O and T represent peaks exclusive to the rhombohedral, orthorhombic and tetragonal phases, respectively.

FIG. 3. (color online): Rietveld fitted x-ray powder diffraction patterns at 20 K of (a) $x = 0.70$ fitted with $R3m$, (b) $x = 0.80$ fitted with $P4mm + Amm2$, (c) $x = 0.80$ fitted with $P4mm + Amm2 + R3m$, (d) $x = 0.825$ fitted with $P4mm + R3m$, (e) $x = 0.825$ fitted with $P4mm + Amm2$, and (f) $x = 0.89$ fitted with $P4mm$ models. In each panel, the small open red circles correspond to observed pattern. The calculated pattern is shown with continuous (black) lines. The vertical bars correspond to calculated Bragg peak positions. The difference profile is shown at the bottom of the panel with continuous (blue) line. The arrow in the inset of Panel (b) highlights the inadequacy of the $P4mm + Amm2$ model to account for the shoulder peak. Similarly, the arrow in the inset of panel (d) highlights the inadequacy of the $P4mm + R3m$ model to account for the hump corresponding to the “O” peak in Fig 2(d).

FIG. 4. (color online): Thermal evolution of the Cartesian components of the spontaneous polarization in BCTZ-0.845 upon heating. Panels a and b show simulation results for CMC and PIQMC, respectively.

TABLE I. X-ray powder diffraction refined structural parameters, thermal factor $B(\text{\AA}^2)$, and agreement factors for annealed powder $0.18\text{Ba}(\text{Ti}_{0.8}\text{Zr}_{0.2})\text{O}_3-0.82(\text{Ba}_{0.7}\text{Ca}_{0.3})\text{TiO}_3$ using Tetragonal($P4mm$) + orthorhombic($Amm2$) + Rhombohedral ($R3m$) phase coexistence models at temperature 20 K.

Space group		$P4mm$				$Amm2$				$R3m$			
Atoms	x	y	z	B(Å ²)	x	y	z	B(Å ²)	x	y	z	B(Å ²)	
Ba/Ca	0.000	0.000	0.000	0.44(3)	0.00	0.000	0.000	0.29(1)	0.000	0.000	0.000	0.76(6)	
Ti/Zr	0.500	0.500	0.499(4)	0.49(6)	0.500	0.000	0.493(2)	0.47(4)	0.000	0.000	0.477(2)	0.17(1)	
O1	0.500	0.500	0.016(0)	0.19(3)	0.000	0.000	0.583(3)	0.17(0)	0.312(0)	0.181(0)	0.653(5)	0.1(0)	
O2	0.500	0.000	0.488(1)	0.25(0)	0.500	0.265(2)	0.288(6)	0.08(0)					
a = 3.9508(0) Å					a = 3.9596(2) Å					a = 5.6204(1) Å			
c = 4.0125(0) Å					b = 5.6191(0) Å					c = 6.9041(0) Å			
					c = 5.6352(3) Å								
Agreement factors:				R _p : 10.3 R _{wp} : 12.4 R _{exp} : 10.39				Chi ² : 1.43					

TABLE II. Phase fractions (in %) of the different phases for different compositions of BCTZ- x at 20 K, as extracted from Rietveld analysis on measured XRD spectra. The estimated phase fractions is within $\pm 5\%$

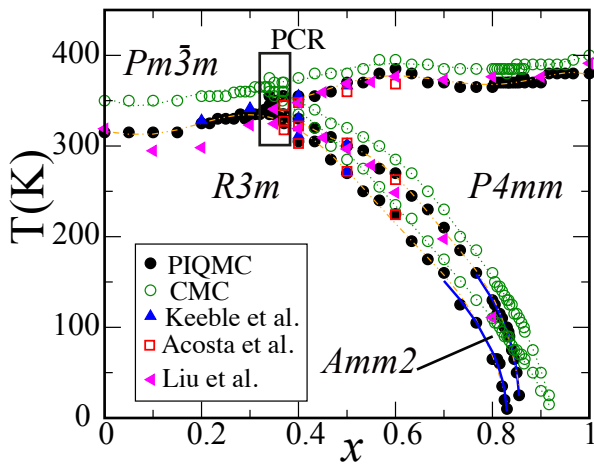
x composition	$P4mm$	$Amm2$	$R3m$
0.70	0	0	100
0.80	15	45	40
0.82	30	50	20
0.825	35	65	0
0.835	55	45	0
0.845	62	38	0
0.87	72	28	0
0.89	100	0	0

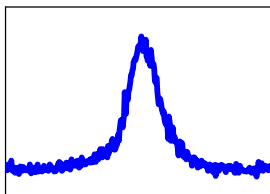
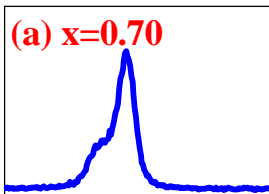
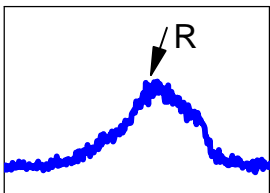
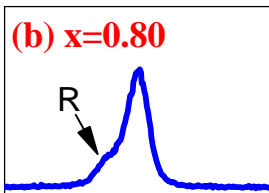
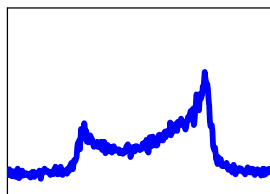
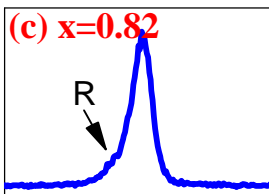
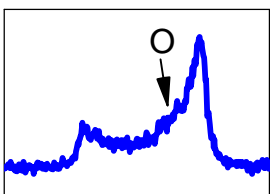
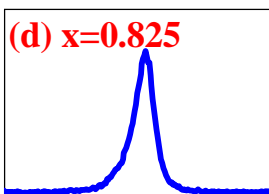
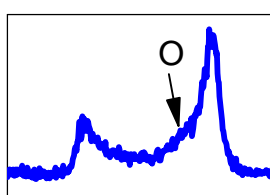
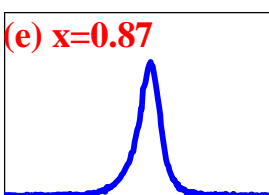
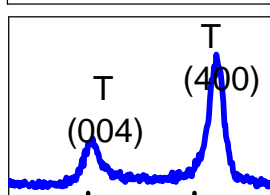
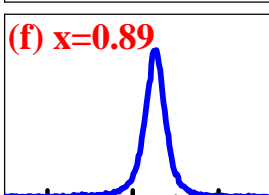
FIG. 5. (color online): Cartesian components of fluctuations of the local dipoles *versus* temperature in BCTZ-0.845 upon heating, as predicted in PI-QMC simulations along the x, y, z - axes in panels (a), (b), and (c), respectively.

FIG. 6. (color online): Cartesian components of fluctuations of the local dipoles *versus* composition at T=5K as predicted in PI-QMC simulations, along the x, y, z - axes in panels (a), (b), and (c), respectively.

FIG. 7. (color online): Temperature dependency of the percentage of dipoles belong to R, O and T clusters in BCTZ- x with $x = 0.845$, as predicted by CMC (panel (a)) and PIQMC (panel (b)) simulations. The inset in panel (a) shows a 3D snapshot of local dipoles (purple arrows) at 60 K within CMC simulations, and indicate a single R cluster. The inset of Panel (b) shows similar data at 60 K too, but for the PI-QMC simulations. This last inset reveals the existence of single O cluster, inside which local dipoles are aligned along $[1\ 0\ 1]$ (orange arrows), as well as a small percentage of local dipoles (purple arrows) belonging to two R clusters, namely for which the dipoles lie along $[1\ 1\ 1]$ and $[1\ \bar{1}\ 1]$, respectively.

FIG. 8. (color online): Strain in $\langle 111 \rangle$ basis, i.e., $\delta l_{\langle 111 \rangle}$, vs. magnitude of applied electric field parallel to $\langle 111 \rangle$ direction, in PI-QMC and CMC, for composition $x = 0.845$ and at 60 K. Dashed line is the linear fit into CMC results, while blue solid line is similar fit into PI-QMC simulations results. Note that in case of PI-QMC for fields larger than 8×10^6 V/m the system undergoes phase transition from $Amm2$ -to- $R3m$.



$\{222\}_{pc}$ $\{400\}_{pc}$ **(a) $x=0.70$** **(b) $x=0.80$** **(c) $x=0.82$** **(d) $x=0.825$** **(e) $x=0.87$** **(f) $x=0.89$** 

83 84 85

100 102

 2θ (degree)

Intensity (arb. unit)

